

# 5-DOF Microcoil Positioning System Utilizing Single-Axis Electromagnetic Transmitter

Yonggan Yan , Shuxiang Guo , *Fellow, IEEE*, Bingzhi Shen, Chuqiao Lyu , Mingchao Ding, Pengfei Yang , Yongwei Zhang , Yongxin Zhang , and Jianmin Liu 

**Abstract**—The lack of 3-D localization impedes the advancement of various intracorporeal medical devices. Developing an occlusion-free, small-sized, and high-precision positioning system remains a significant challenge in the practical application of interventional robotics. In this article, a novel 5-degree of freedom (DoF) positioning system utilizing single-axis electromagnetic field excitation coil is designed to locate a microcoil with a size of  $\phi 1.45 \times 5$  mm. An XGBoost-based induced electromotive force (EMF) prediction model is proposed to correct the deviation of the magnetic dipole model near the excitation source. Employing the model, a positioning dataset under rotating magnetic field is synthesized. Subsequently, a CNN-LSTM based 5-DoF positioning model is designed and trained, and the transmitting coil speed characteristics of the model were experimentally verified. Evaluation experiments for the two models are performed separately. The results demonstrate the XGBoost-based EMF prediction model improved the prediction accuracy by 34.4% compared to the conventional magnetic dipole model. The static average localization error of the 5-DoF positioning model is 2.53 mm and the orientation error is  $2.24^\circ$  within the  $\phi 150 \times 70$  mm volume. The dynamic tracking experimental results indicate that the localization tracking error is 4.25 mm and the orientation error is  $3.44^\circ$ , which are 62% and 78%

higher than the Levenberg–Marquardt algorithm. The navigation experiment conducted in a coronary artery phantom demonstrated the potential for use in narrow tracts.

**Index Terms**—5-DoF positioning, electromagnetic tracking, localization, microcoil positioning, surgical navigation.

## I. INTRODUCTION

**O**CCCLUSION-FREE positioning system with small-sized sensors has broad prospects in various domains, especially in the interventional surgery [1]. It provides accurate and multidegree-of-freedom position navigation for doctors, and improves the success rate and efficiency of surgery. Robot-assisted vascular interventional surgery (VIS) can isolate surgeons and patients through the leader-follower robotic system. It solves the problems of surgeons being harmed by X-ray radiation generated by the digital subtraction angiography, and insufficient operating accuracy [2]. Traditional VIS relies on the surgeons' extensive anatomical knowledge and long-term experience. Surgeons judge the physical status of the intravascular instruments based on the 2-D X-ray images and the hand haptic feedback [3]. However, the robot-assisted remote surgery reduces the effectiveness of haptics, forcing surgeons to rely almost entirely on 2-D images. Incomplete surgical information increases the surgery risk [4].

Accurate 3-D positioning of instruments can improve the success rate of the surgery. The magnetic field can be used to calculate the pose of the induction coils due to its inherent penetrability. Magnetic field-based positioning method is mainly divided into the Hall sensor-based positioning method [5], [6], [7] and the electromagnetic positioning method [8], [9]. Depending on the positioning object, Hall sensor-based positioning method is further divided into permanent magnet positioning method [5], [6], [7] and Hall sensor positioning method [10], [11], [12]. The permanent magnet positioning method senses the magnetic field characteristics around the permanent magnet based on a multisensor array. However, it is challenging in terms of the number and volume of localized objects. So it is often used for larger objects such as guided vehicles and robotic arms [5], [6], [7], [13]. The Hall sensor positioning method uses the Hall sensor as the positioning object and can locate multiple objects. Hall sensor integrates Hall elements, amplifiers and so on. So the sensor is hard to be less than 3 mm [10], [11], [12]. Electromagnetic positioning method is based on the electromagnetic induction effect. A rigid body

Received 24 September 2024; revised 8 January 2025 and 13 February 2025; accepted 18 March 2025. Recommended by Technical Editor A. K. Hoshiar and Senior Editor M. Indri. This work was supported in part by the National Natural Science Foundation of China under Grant 61703305, and in part by the National High-tech Research and Development Program (863 Program) of China under Grant 2015AA043202. (Corresponding author: Shuxiang Guo.)

Yonggan Yan, Bingzhi Shen, and Chuqiao Lyu are with the Aerospace Center Hospital, School of Life Science and the Key Laboratory of Convergence Medical Engineering System and Healthcare Technology, Ministry of Industry and Information Technology, Beijing Institute of Technology, Beijing 100081, China.

Shuxiang Guo is with the Department of Electronic and Electrical Engineering, Southern University of Science and Technology, Shenzhen, Guangdong 518055, China, and also with the Aerospace Center Hospital, School of Life Science and the Key Laboratory of Convergence Medical Engineering System and Healthcare Technology, Ministry of Industry and Information Technology, Beijing Institute of Technology, Beijing 100081, China (e-mail: guo.shuxiang@sustech.edu.cn).

Mingchao Ding is with the Department of Peripheral Vascular Intervention, Aerospace Center Hospital, School of Life Science, Beijing Institute of Technology, Beijing 100081, China.

Pengfei Yang, Yongwei Zhang, Yongxin Zhang, and Jianmin Liu are with Neurovascular Center, Changhai hospital, Naval Medical University, Shanghai 200433, China.

Color versions of one or more figures in this article are available at <https://doi.org/10.1109/TMECH.2025.3554246>.

Digital Object Identifier 10.1109/TMECH.2025.3554246

in 3-D space has 6 degrees of freedom (DoFs), so at least 6 features need to be collected to uniquely determine its pose. The existing electromagnetic positioning systems generally consist of three orthogonal transmitting coils run through different frequencies alternating currents and three orthogonal sensing coils. The collected induced electromotive force (EMF) of the sensing coil is decoupled according to frequency to obtain the induction characteristics between coils. Then the location and orientation of the sensing coil is calculated. However, the sensor with three orthogonal coils is too large to be applied *in vivo*. Therefore, the single-axis sensing coil has the potential for miniaturization [14]. More than 5 transmitting coil arrays with different frequencies alternating currents can locate single-axis sensing coils, and more transmitting coils provide more induced signal features for locating the sensing coils accurately [9].

The circular integral model for representing the coil magnetic field is too complex to be solved analytically. So the magnetic dipole model, which can simply describe the spatial magnetic field distribution of magnetic bodies, is widely used [8]. The existing magnetic dipole model-based positioning methods are applicable when the radius vector norm of the sensing coil from the transmitting coil is much larger than the diameter of the transmitting coil (over four times), otherwise the error will be large. Therefore, calibration algorithms are studied. The Levenberg–Marquardt (LM) algorithm is an iterative method used for optimizing nonlinear least squares problems. It is used to adjust the parameters of the magnetic dipole model [9]. However, the accuracy and efficiency of the LM algorithm are sensitive to initial values and prone to accumulating errors and falling into local optima. The existing problems are summarized as follows.

- 1) Although increasing the number of magnetic field excitation sources can enhance the signal features of sensing coils to improve positioning accuracy, it faces limitations in being large-scale deployed in practical applications.
- 2) The positioning method based on the magnetic dipole model can be applied to long-distance spaces [15], which is contrary to the magnetic flux density that rapidly attenuates with the radius vector norm of the two coils.
- 3) Nonlinear optimization algorithms are easily affected by initial values during the positioning process, resulting in significant pose tracking errors.

The contributions of this work are summarized as follows.

- 1) An electromagnetic positioning system with a single-axis transmitter and a single-axis sensing coil is developed. The rotating magnetic field transmitter significantly enhances effective signal features. The compact sensing coil, with a size of  $\phi 1.45 \times 5$  mm, enables potential applications in narrow tracts.
- 2) An XGBoost-based induced EMF prediction model is proposed to correct the deviation of the magnetic dipole model in the near excitation source space, improving overall positioning accuracy.
- 3) A novel method efficiently generates a comprehensive dataset for sensing coil positioning, thereby reducing the time and effort needed for data collection.

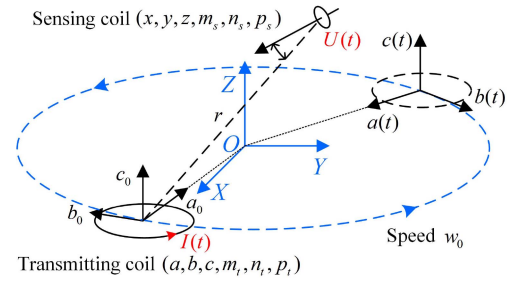


Fig. 1. Positioning method utilizing a rotating transmitting coil.

- 4) A CNN-LSTM based positioning model is designed to predict 5-DoF localization and orientation of the sensing coil accurately.

The rest of this article is organized as follows. Section II introduces the developed electromagnetic positioning device. The 5-DoF positioning model is designed in Section III. Section IV introduces the evaluation experiments. Finally, Section V concludes this article.

## II. ELECTROMAGNETIC POSITIONING DEVICE DEVELOPED

### A. Theoretical Model

Assume that the location and orientation of the magnetic dipole in the Cartesian coordinate system is  $(a, b, c, m_t, n_t, p_t)$ , the magnetic flux intensity  $\mathbf{B}$  at point  $(x, y, z)$  is written as

$$\mathbf{B} = k \left( \frac{3(\mathbf{H}_0 \cdot \mathbf{P})\mathbf{P}}{r^5} - \frac{\mathbf{H}_0}{r^3} \right) \quad (1)$$

where  $\mathbf{H}_0 = (m_t, n_t, p_t)$ ,  $\mathbf{P} = (x - a, y - b, z - c)$ .  $k$  is a constant related to the excitation source.  $r$  is the distance between  $(a, b, c)$  and  $(x, y, z)$ , i.e., the radius vector norm  $r = \|\mathbf{P}\|$ . The three components of the magnetic flux intensity at  $(x, y, z)$  can be calculated by

$$\begin{cases} B_x = k \left\{ \frac{3[m_t(x-a) + n_t(y-b) + p_t(z-c)](x-a)}{r^5} - \frac{m_t}{r^3} \right\} \\ B_y = k \left\{ \frac{3[m_t(x-a) + n_t(y-b) + p_t(z-c)](y-b)}{r^5} - \frac{n_t}{r^3} \right\} \\ B_z = k \left\{ \frac{3[m_t(x-a) + n_t(y-b) + p_t(z-c)](z-c)}{r^5} - \frac{p_t}{r^3} \right\} \end{cases} \quad (2)$$

To expand the effective signal features, an excitation source based on a rotating single-axis transmitting coil is proposed, as shown in Fig. 1. The rotating transmitter is equivalent to many coils on the moving trajectory and activated one by one. A coordinate system in which the  $c$ -axis is the axis direction of the transmitting coil is established.  $(m_t, n_t, p_t) = (0, 0, 1)$ . An alternating current runs through the transmitting coil, and an alternating electromagnetic field is generated, where  $I(t) = I_z \cdot \sin(2\pi ft)$ .  $f$  is the frequency. Bringing the orientation vector of the transmitting coil into (2), the magnetic flux intensity at the sensing coil is obtained

$$\begin{cases} B_x(t) = k_1 \left\{ \frac{3[x-a(t)][z-c(t)]}{r^5(t)} \right\} \\ B_y(t) = k_1 \left\{ \frac{3[y-b(t)][z-c(t)]}{r^5(t)} \right\} \\ B_z(t) = k_1 \left\{ \frac{3[z-c(t)]^2}{r^5(t)} - \frac{1}{r^3(t)} \right\} \end{cases} \quad (3)$$

where  $k_1$  is related to the magnetic moment and turns of the transmitting coil. The radius vector norm  $r(t)$  is written as

$$r(t) = \sqrt{(x - a(t))^2 + (y - b(t))^2 + (z - c(t))^2}. \quad (4)$$

The sensing coil is induced in the alternating magnetic field and generates the EMF  $U(t) = A \cdot \sin(2\pi ft)$ . Assume that the pose of the sensing coil is  $(x, y, z, m_s, n_s, p_s)$ . The induced EMF amplitude  $A$  can be expressed as

$$A = k_2[m_s B_x(t) + n_s B_y(t) + p_s B_z(t)] \quad (5)$$

where  $k_2$  is a parameter related to the turns and geometry of the transmitting coil. Equation (3) is brought into (5) to obtain the induced EMF amplitude, as shown in Eq. (6) at the bottom of this page. The electromagnetic positioning device has only one excitation source, which simplifies the signal processing process such as signal decoupling based on frequency. Therefore, the positioning model only needs to capture the amplitude features of the induced EMF to predict the sensing coil pose.

### B. Mechanical Structure Design

Fig. 2(a) displays the developed electromagnetic positioning device. The sensing coil is coaxially embedded in the proximal end of a steerable catheter [16] to measure the pose of the catheter tip. The transmitting coil rotates uniformly around an axis and generates high-frequency alternating electromagnetic fields. The sensing coil in the magnetic field generates induced EMF signal. It is transmitted to the signal capturer through a single axis shielded wire with a diameter of 0.2 mm and length of 1 m. And the signal sequence is collected in real-time as input for predicting the pose of sensing coil. In previous work, we designed a catheter manipulation device named PG2 gripper for VIS, as shown in Fig. 2(b) and (c) [17], [18]. The gripper has two opening fingers that can reach, grasp, and twist thin cylinders with different diameters. A PG2 gripper and a tendon actuator are mounted on a linear slide. The two manipulators map the surgeon's hands movements in the leader side, such as advancing, retracting, twisting, clamping, and releasing. Fig. 2(d) displays the designed magnetic field generator. The transmitting coil is installed on the rotating sun gear plate and rotates around the gear axis. The sun gear meshes with the drive gear, which is driven by a servo motor. The other side of the sun gear drives an encoder through gear transmission. The measured angle multiplied by the transmission ratio is the angle of the sun gear. Traditional brush-based electric slip rings inevitably produce noise on analog signals due to contact impedance fluctuations during rotating. To ensure the quality of high-frequency alternating current running into the rotating transmitting coil, a mercury-based slip ring is used. It has low and stable contact resistance and can be used in high-speed applications. Three flange cantilever structures are used to axially fix the three gears. The outer diameter of the magnetic field generator is 220 mm.

Fig. 2(f1), (f2) show the spatial magnetic field distribution in the sagittal plane of a single-layer densely wound coil run through a current of 0.6 A. The simulation results and (6) shown at the bottom of this page, indicate that the magnetic flux intensity above the coil attenuates with a cubic rule almost along the sphere radial direction, of which center is the geometric center of the coil. Due to the inherent magnetic field attenuation characteristics, the transmitting coil is installed obliquely and points toward the workspace. It increases the displacement variation of the sensing coil along the direction of the gradient attenuation of the magnetic field as the transmitting coil rotates, which is conducive to improving horizontal positioning accuracy.

### C. Electromagnetic Coils Design

To ensure that the sensing coil is induced with sufficient EMF in the workspace, parameters of the transmitting coil and sensing coil are designed. Fig. 2(e) displays the cylindrical workspace and two coils located at the extreme position with the maximum radius vector norm. The transmitting coil is placed horizontally. It should be noted that the tilted transmitting coil induces a larger EMF in the sensing coil at the extreme position. Therefore, it is conservative to calculate and lectotype when the transmitting coil is installed horizontally. Based on (1), the magnetic field generated by the transmitting coil at  $P_s$  is written as

$$\mathbf{B}_s = \frac{\mu_0 N_t}{4\pi} \left( \frac{3(\mathbf{m}_t \cdot \mathbf{r}_s)\mathbf{r}_s}{r^5} - \frac{\mathbf{m}_t}{r^3} \right) \quad (7)$$

where  $\mathbf{B}_s$  represents the magnetic flux intensity at  $P_s$ ,  $\mu_0$  is the permeability of vacuum,  $\mu_0 = 4\pi \times 10^{-7} \text{N/A}^2$ ,  $N_t$  represents the turns of the transmitting coil,  $\mathbf{m}_t$  represents the magnetic moment vector of the magnetic dipole,  $\mathbf{m}_t = I_t S_t \mathbf{k}$ , and  $\mathbf{k} = (0, 0, 1)$ .  $I_t(t) = A_t \sin(w_t t)$ ,  $w_t = 2\pi \times 10^6 \text{ rad/s}$ ,  $S_t = \pi r_t^2$ ,  $r_t$  is the radius of the transmitting coil. Take  $A_t = 0.6 \text{ A}$ , which is the balance between the magnetic field strength and the ability of the power amplifier (ADA4870, ZONRI, China) to dissipate the heat generated by the reactive power.  $\mathbf{r}_s$  is the radius vector from the transmitter to the sensing coil,  $r = \|\mathbf{r}_s\|$ . The poses of the two coils are brought into (7), and the simplified result is

$$\|\mathbf{B}_s\| = 17.8958 \mu_0 N_t r_t^2 \cdot \sin(2\pi \times 10^6 t). \quad (8)$$

The induced EMF of the sensing coil is determined by the change rate of the magnetic flux and is written as

$$\varepsilon^{ts} = -N_s \frac{d(\mathbf{B}_s \cdot \mathbf{S}_s)}{dt} \quad (9)$$

where  $\varepsilon^{ts}$  represents the induced EMF of the sensing coil, and  $N_s$  is the turns of the sensing coil. Taking the effective diameter of the sensing coil to be 1.4 mm,  $N_s = 1000$ .  $\mathbf{S}_s$  is the surface of the coil,  $\|\mathbf{S}_s\| = \pi r_s^2$ . The signal capturer can capture EMF greater than 0.2 mV, i.e.,  $\varepsilon_{\max}^{ts} \geq 0.2 \text{ mV}$ . The condition is brought

$$A = k \left\{ \frac{3m_s(x-a)(z-c) + 3n_s(y-b)(z-c) + p_s[3(z-c)^2 - r^2(t)]}{r^5(t)} \right\}. \quad (6)$$

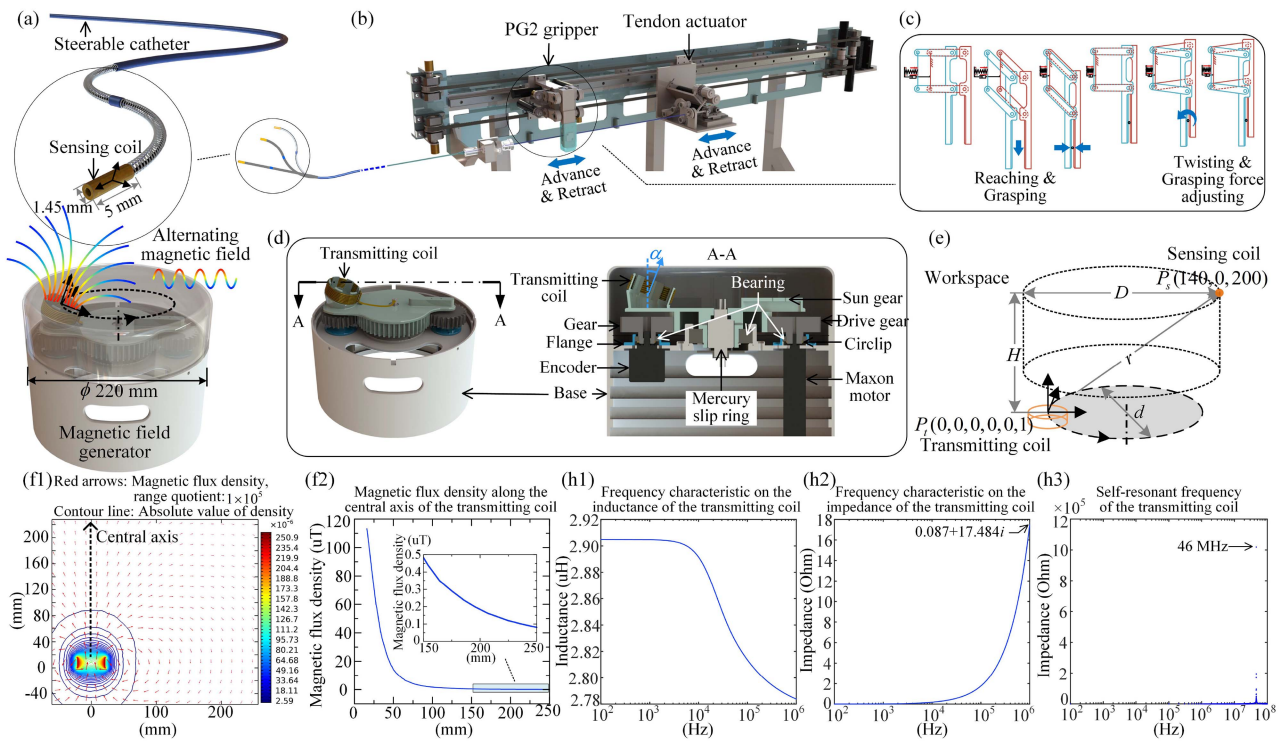


**Fig. 2.** Developed electromagnetic positioning device. (a) The electromagnetic positioning device. (b) The VIS robotic system. (c) Manipulating states of the PG2 gripper. (d) Mechanical structure of the magnetic field generator. (e) The positioning workspace.  $D = 150$  mm,  $H = 200$  mm. The rotation diameter of the transmitting coil is  $d = 130$  mm. The two coils are located at the maximum point of the radius vector norm. (f1,f2) The spatial magnetic field of the transmitting coil. (h1,h2) Frequency characteristic of the transmitting coil. (h3) First-order self-resonant frequency of the transmitting coil.

into (9)

$$N_t r_t^2 \geq 9.1954 \times 10^{-4}. \quad (10)$$

The effective diameter of the transmitting coil is set to 44 mm, i.e.,  $r_t = 0.022$  m. The turns need to satisfy  $N_t \geq 1.9$ . As the signal frequency increases, the inductance loss of the coil gradually increases. And the interturn capacitance of the coil is crucial to the high-frequency characteristics. The frequency influence on the inductance and impedance of the transmitting coil with 7 turns is plotted in Fig. 2(h1), (h2). With the frequency increasing from 10 kHz to 1 MHz, the transmitting coil inductance slightly decreases to 2.784  $\mu\text{H}$  while the impedance increases rapidly to 17.484  $\Omega$ . The required excitation voltage exceeds 21 V<sub>pp</sub>. A larger frequency can enhance the induced signal, but increases the output power of the power amplifier. The reactive power generated by inductive loads also increases the heating of the amplifier. Therefore, the turns of the transmitting coil are a tradeoff between the magnetic flux density and the power load. Fig. 2(h3) displays that the first-order self-resonant frequency of the transmitting coil is 46 MHz, which is much greater than excitation frequency of 1 MHz. The parameters of the two coils are summarized in Table I.

**TABLE I**  
PARAMETERS OF THE TWO COILS

Coils	Turns	Diameter (mm)	Frequency (MHz)	Impedance ( $\Omega$ )
Sensing coil	1000	1.4	1	7
Transmitting coil	7	44	1	17.484

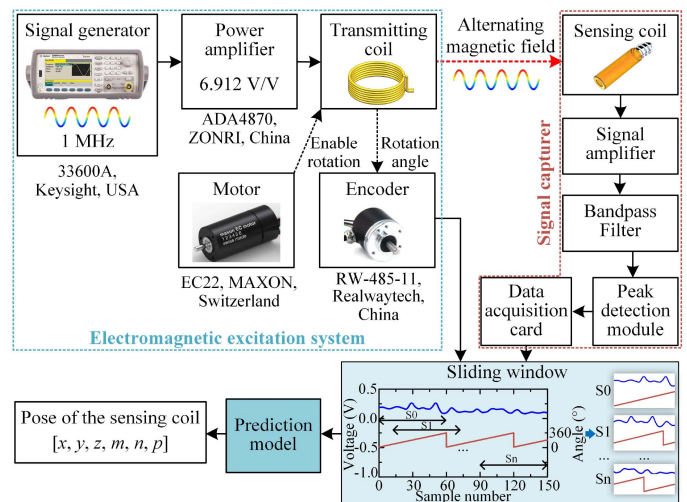


**Fig. 3.** Electrical System Diagram. A rotating alternating magnetic field is excited. The signal capturer captures the EMF of the sensing coil. The positioning model extracts the signal features to predict the sensing coil pose.

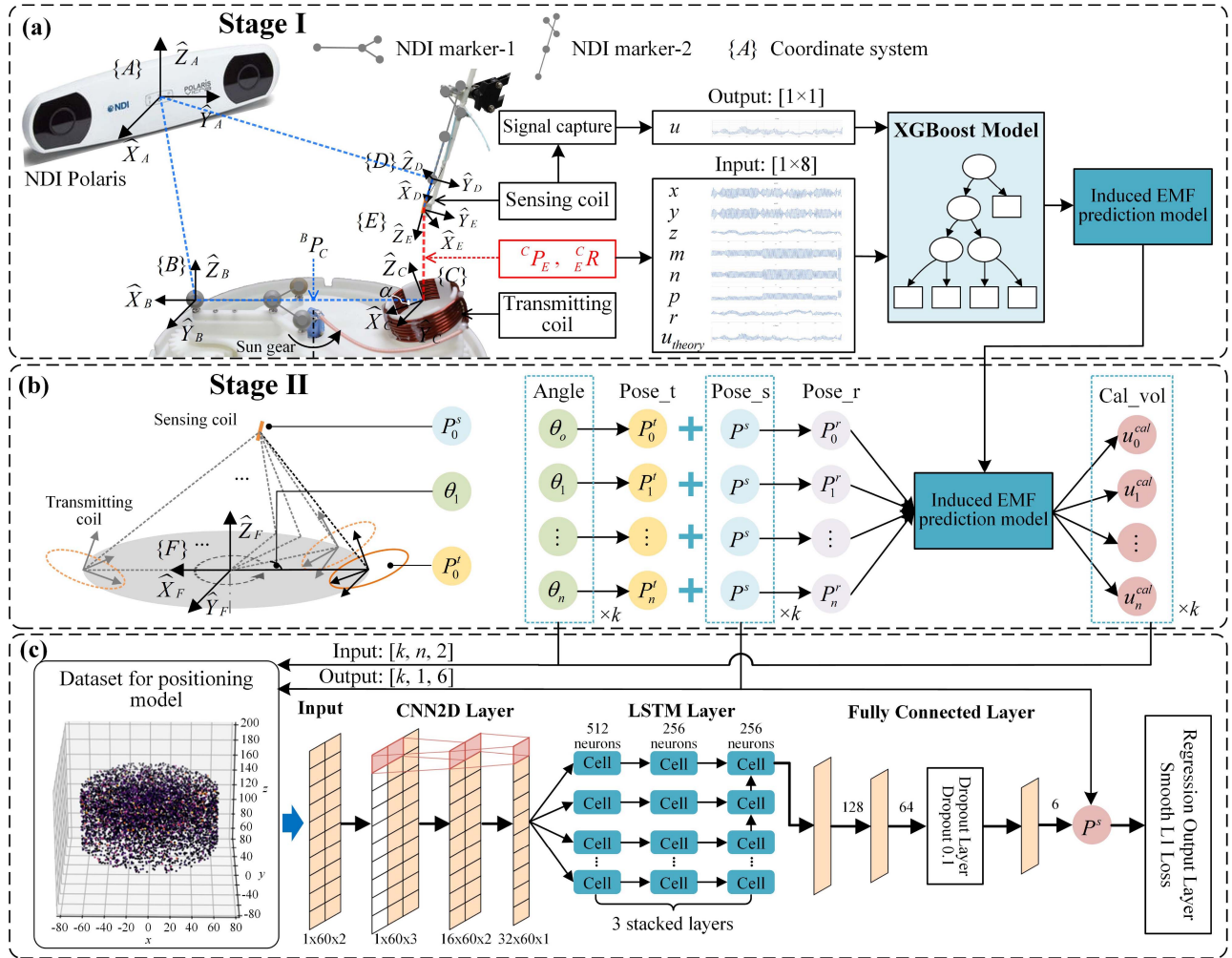


Fig. 4. Schematic diagram of the proposed electromagnetic positioning model. (a) XGBoost-based induced EMF prediction model. (b) Positioning model dataset generation. (c) CNN-LSTM-based 5-DoF electromagnetic positioning model.

## D. Electrical System Developed

The developed electrical system is shown in Fig. 3. A signal generator generates a 1 MHz sinusoidal signal. The signal is amplified 6.912 times by a power amplifier. The amplified current runs through the transmitting coil to excite a high-frequency alternating magnetic field. The sensing coil is induced in the magnetic field. The weak induced EMF is amplified 500 times by an operational amplifier. To reduce the influence of electromagnetic interference, an active bandpass filter is adopted. On the one hand, active filters without inductors do not require magnetic shielding. On the other hand, it reduces the loss of signals passing through cascaded electronic modules. The filtered signal amplitude effectively represents the induction intensity of the two coils, so a peak detection module is adopted to detect the amplitude. The analog signals are collected by a data acquisition card. The rotating angle of the transmitting coil is collected by an encoder. The motion angle and induced EMF peak signal are combined into the original dataset, and a sliding window is employed to update the input data of the positioning model.

## III. ELECTROMAGNETIC POSITIONING MODEL

A novel electromagnetic positioning model is proposed and established in three steps, as shown in Fig. 4: 1) establish an accurate induced EMF prediction model for the sensing coil; 2) simulating various motion states of the transmission coil and transforming spatial coordinates, a dataset is generated based on the induced EMF prediction model; c) train and establish the 5-DoF positioning model.

### A. Induced EMF Prediction Model

The magnetic dipole model approximately explains the peripheral magnetic field of the excitation source. The fitting is inaccurate in the near source space. In addition, factors such as gap winding and irregular circle of the transmitting coil also limit the fitting effect. XGBoost model is a machine learning algorithm based on decision trees, which is implemented based on the gradient boosting framework. Compared with other regression algorithms, XGBoost model has better regression accuracy and

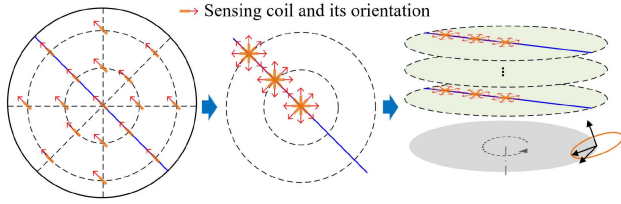


Fig. 5. Data collection rule for the EMF prediction model.

faster calculation speed [19]. Therefore, an XGBoost-based induced EMF prediction model is established as shown in Fig. 4(a). An optical positioning system NDI Polaris is employed to calculate the relative pose of the transmitting coil and the sensing coil in real-time. NDI marker-1 and the transmitting coil are installed on the rotating sun gear, and the line connecting the two crosses the rotation axis. The NDI marker-2 and sensing coil are installed on a rigid body. Coordinate systems  $\{A-E\}$  are established in Polaris, marker-1, transmitting coil, marker-2, and sensing coil, respectively. Among them,  $\{A\}$  is the global coordinate system. Quaternion is used to transform the poses of the objects. The relative location of  $\{C\}$  to  $\{A\}$  is calculated as

$${}^A P_C = {}^A Q * {}^B P_C * {}^A Q^* + {}^A P_B. \quad (11)$$

The orientation  ${}^A Q$  is written as:

$${}^A Q = {}^B Q * q_y^\alpha. \quad (12)$$

Similarly,  $\{E\}$  moves  ${}^D P_E$  along the positive direction of  $\hat{X}_D$  and rotates  $90^\circ$  counterclockwise around  $\hat{Y}_D$ . The relative location  ${}^A P_E$  of the sensing coil to  $\{A\}$  is written as

$${}^A P_E = {}^A Q * {}^D P_E * {}^A Q^* + {}^A P_D. \quad (13)$$

The orientation  ${}^A Q$  relative to  $\{A\}$  is written as

$${}^A Q = {}^D Q * q_y^{90}. \quad (14)$$

Then the relative location of the sensing coil  $\{E\}$  to the transmitting coil  $\{C\}$  can be calculated as

$${}^C P_E = {}^A Q^* * ({}^A P_E - {}^A P_C) * {}^A Q \quad (15)$$

where the last three parameters of  ${}^C P_E$  are the relative coordinates. The relative pose of the sensing coil  $\{E\}$  to the transmitting coil  $\{C\}$  can be calculated as

$${}^C R = {}^A Q^* * {}^A Q \quad (16)$$

where  ${}^C R$  is further calculated to obtain the orientation vector  ${}^C V$  of  $\hat{Z}_E$  relative to  $\{C\}$ . The induced EMF measured by the signal capturer is the output of the EMF prediction model. The location  ${}^C P_E$  and orientation  ${}^C V$  are inputs. The magnetic dipole model-based induced EMF  $u_{theory}$  is an important input feature. In addition, the radius vector norm  ${}^C r$  representing the distance between the two coils is an input feature.

The transmitting coil is rotating during dataset acquisition, so the contour planes within the workspace contain a number of redundant data points. To improve the collection efficiency and integrity of the dataset, a data collection rule is set, as shown in Fig. 5. The centrally symmetrical sensing coils on the

TABLE II  
ADJUSTED HYPERPARAMETER RESULTS OF THE XGBOOST MODEL

max_depth	n_estimators	MAE (mV)	MedAE (mV)	Size (Kb)
9	120	2.15	1.56	1084
11	120	2.08	1.47	1463
<b>11</b>	<b>150</b>	<b>2.01</b>	<b>1.43</b>	<b>1656</b>
11	180	2.00	1.48	1837
13	120	2.07	1.49	1688

Bold entries represent the optimal hyperparameters of the XGBoost model and the corresponding model performance.

TABLE III  
FEATURE ABLATION EXPERIMENT

Case	Position (x,y,z)	Orientation (Quaternion)	Radius vector (r)	$u_{theory}$	MAE (mV)	MedAE (mV)
1	✓	✓	×	×	3.30	2.33
2	✓	×	×	✓	2.89	2.05
3	×	✓	×	✓	3.40	2.46
4	×	×	✓	✓	4.60	3.28
5	×	×	×	✓	5.09	3.61
6	✓	✓	✓	✓	<b>2.01</b>	<b>1.43</b>

Bold entries represent the lowest values of MAE and MedAE.

concentric circles can be equivalently rotated to one point. Even though the orientations of the sensing coils remain relative to the global coordinate, the equivalent orientation rotates relative to the rotation center. In the workspace, 6 contour surfaces spaced 10 mm apart are set. There are two sets of concentric circles on each contour surface with diameters of 70 mm and 140 mm. Eight sample points are set at intervals of  $45^\circ$  on each concentric circle. One rotation of the transmitting coil is one acquisition cycle. The relative locations and orientations of the two coils and EMF are collected in real-time and combined into the original dataset.

As shown in Fig. 4(a), the calculated input features  $(x, y, z, m, n, p, r, u_{theory})$  and the induced EMF amplitude  $u$  as the output formed a dataset containing 30000 data. The XGBoost model was used to fit them with the loss function of the mean square error (MSE). Table II presents the adjusted model hyperparameter results. Although the 11-layer decision tree with 180 iterations has a slightly lower mean absolute error (MAE), the 11-layer decision tree with 150 iterations is preferred due to its lower median absolute error (MedAE) and storage memory. In the ablation study, we evaluated the impact of various features on the performance of the model by progressively removing input features. The experimental results were shown in Table III. The model incorporating all features performed best, with a MAE of 2.01 mV and a MedAE of 1.43 mV. When the  $u_{theory}$  was removed, the model's MAE increased to 3.30 mV, indicating that this feature played a significant role in improving prediction accuracy. The other features still contributed significantly to the model's overall performance. Upon further removal of orientation information, the MAE increased to 2.89 mV, suggesting that spatial position information and radius vector were important for accuracy. With the simultaneous removal of spatial position and orientation information, the error increased to 3.40 mV, confirming the crucial role of spatial features in the model's predictions. This study demonstrates that integrating diverse feature types significantly enhances model performance.

## B. Training Dataset Generation for the Positioning Model

The sensing coil has 5-DoF, i.e., the location and orientation vector  $(x, y, z, m, n, p)$ . It means that the positioning model prediction parameters contain at least 5 independent variables, which greatly increases the difficulty of regression fit. In addition, multivariable regression also greatly increases the workload of datasets collection. It is difficult to ensure uniform data distribution and sufficient data volume. To solve this problem, a dataset generation model is designed. First, a large amount of random pose labels are generated in the workspace based on the Monte Carlo method. The feature data of each label is predicted based on the EMF prediction model. Then, the labels and features are combined as the electromagnetic positioning model dataset.

The coordinate system  $\{F\}$  of the electromagnetic positioning device is established with the rotation center of the transmitting coil as the origin, as shown in Fig. 4(b). The rotation angle of the transmitting coil is  $\theta$ . The location and orientation of the transmitting coil in  $\{F\}$  are written as

$${}^F P_\theta^t = q_z^\theta * {}^F P_0^t * (q_z^\theta)^* \quad (17)$$

$${}^F Q_\theta^t = q_0 * q_z^\theta * q_y^\alpha \quad (18)$$

Given a sensing coil pose  $({}^F P^s, {}^F Q^s)$ . Based on (15) and (16), the relative location and orientation  $({}^t P_\theta^s, {}^t Q_\theta^s)$  of the two coils can be calculated. The calculated features are input into the EMF prediction model to predict the induced EMF  $u^{cal}$ .

Each rotation cycle selects 60 points evenly distributed to generate feature data of a sensing coil pose, that is,  $n = 60$ ,  $\Delta\theta = 6^\circ$ . It is equivalent to a magnetic field system with 60 excitation coils, which effectively enhances the signal features. The selection of 60 points per cycle was determined through preliminary testing where it was found to balance comprehensively model prediction accuracy while maintaining computational efficiency. There will be an error between the measured angle and the expected angle, so Gaussian noise is added to each point. Each point has two features of angle  $\theta$  and predicted induced EMF  $u^{cal}$ . Therefore, a set of  $60 \times 2$  feature sequences for a sensing coil pose is generated. Set the workspace to a cylinder with a diameter of 150 mm and a height of 70 mm. Employing the Monte Carlo method, a dataset containing 200 000 randomly sensing coil poses is established within the cylinder for the positioning model.

## C. 5-DoF Electromagnetic Positioning Model

The positioning model needs to capture the correlation between the input feature sequences and each pose label. It is valuable to apply the recurrent neural network (RNN) for regressing the input sequences. Compared with RNN, the long short-term memory neural network (LSTM) with the gated structure, which can solve the problem of gradient disappearance and explosion, is more stable. However, LSTM cannot capture the spatial features. Therefore, combining LSTM with a convolutional neural network (CNN) to capture time series spatial features, i.e., a CNN-LSTM model [20], is effective. The structure of the positioning model is shown in Fig. 4(c).

TABLE IV  
ADJUSTED HYPERPARAMETER RESULTS OF THE POSITIONING MODEL

CNN layers	LSTM layers	Input dimension	Orientation MAE( $^\circ$ )	localization MAE (mm)	Inference time (ms)
0	3	[1, 60]	4.24	4.47	2.94
2	0	[60, 2]	5.31	5.41	1.99
2	2	[60, 2]	3.01	3.11	3.34
<b>2</b>	<b>3</b>	<b>[60, 2]</b>	<b>2.84</b>	<b>2.85</b>	<b>3.50</b>
2	4	[60, 2]	2.91	2.99	4.50

Bold entries represent the optimal hyperparameters of the positioning model and the corresponding model performance.

1) *Offline Training and Estimation*: The CNN-LSTM model is structured with CNN layers, LSTM layers, and fully connected layers. The input to the model consists of 200 000 normalized sequences, generated to reflect various scenarios in electromagnetic positioning. The dataset is split into training and test sets with a ratio of 8:2, ensuring sufficient data for learning and validation. To maintain dimensional consistency, the left side of each sequence is padded with one column of zeros. In the convolutional layers, a  $1 \times 2$  convolution kernel is employed to effectively extract spatial features and intricate patterns from both EMF and angle data, capturing the interdependencies between these two types of inputs. This is particularly important because EMF data and angle data are closely related and together determine the spatial distribution of the electromagnetic field. After the initial feature extraction, a subsequent convolution layer transforms the learned 2-D spatial features into 1-D sequences, making them suitable for temporal analysis by the LSTM layers. The LSTM layers are utilized to analyze these sequences for temporal dependencies, crucial for tracking the location and orientation over time. This transition from spatial to temporal modeling is a critical aspect of the CNN-LSTM architecture, as it enables the model to capture both the spatial distribution and the temporal evolution of the electromagnetic field. The final fully connected layers create a nonlinear mapping between sequence features and output variables. A dropout layer reduces model overfitting. The model employs the Smooth L1 Loss as the cost function, which combines the advantages of MAE loss being insensitive to outliers and the MSE loss being derivative at 0, with fast convergence speed and not easy to run out of training. The proposed model was trained using the PyTorch framework with CUDA acceleration on an NVIDIA GeForce GTX 1070 Ti GPU. The training process consisted of 70 epochs. The optimization of the model parameters took 30 minutes.

To obtain a suitable model structure, the number of CNN layers and LSTM layers were treated as hyperparameters for tuning. Table IV presents the comparison results, which demonstrated that the CNN-LSTM hybrid model outperformed the individual CNN or LSTM models in terms of accuracy. Specifically, the accuracy of the hybrid model improved with the increasing number of LSTM layers. However, due to overfitting, the model with four-layer LSTM exhibited slightly lower accuracy compared to that with three-layer LSTM. Moreover, the model size and inference time increased with the growth of network depth. Considering the tradeoff between accuracy and complexity, a

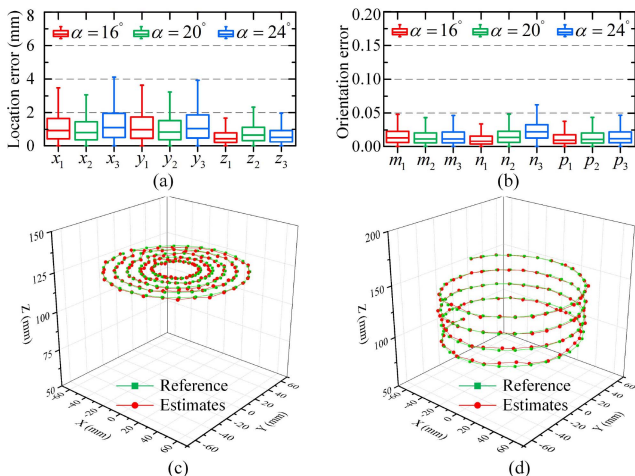


**Fig. 6.** Transmitting coil tilted angle optimization and trajectory prediction. (a,b) localization and orientation accuracy of different tilted angles. (c) Concentric circle trajectories on contour surfaces. Radii: 20:10:60 mm, height: 135 mm. (d) Spiral trajectories. Radius: 60 mm, heights: 95:0.5:155 mm.

two-layer CNN followed by a three-layer LSTM was adopted as the final network architecture.

As mentioned in Section II-B, the tilted transmitting coil can improve positioning accuracy, thus requiring optimization. By leveraging the EMF prediction model, multiple tilted angle datasets can be conveniently generated. The datasets were trained separately. The training results are shown in Fig. 6(a) and (b). The results show that the prediction accuracy is higher when the tilted angle is set to 20°. The prediction results of the expected trajectory by the positioning model with the tilted angle of 20° are shown in Fig. 6(c) and (d). Fig. 6(c) is a set of concentric circle trajectories on contour surfaces with radii ranging from 20 to 60 mm in 10-mm increments and a fixed height of 135 mm. And Fig. 6(d) is a set of spirals with a radius of 60 mm, heights of 95–155 mm with a gradient of 0.5 mm. The results show that the model estimated trajectories are consistent with the expected trajectories. It demonstrates that the proposed positioning model is theoretically feasible.

**2) Online Positioning:** Online positioning is implemented by the trained positioning model. The positioning system measures the rotation angle of the transmitting coil in real-time. When the angle falls within the collection point range, the EMF is collected by the signal capturer. As the transmitter coil rotates, the data sequence is continuously updated. The preprocessing method for the latest sequence data is the same as for offline training. The preprocessed sequence is then fed into the trained CNN-LSTM model for real-time calculation. Finally, the model's output is denormalized to obtain the estimated location and orientation of the sensing coil.

## IV. EXPERIMENTAL RESULTS AND EVALUATION

### A. Experimental Setup

The developed electromagnetic positioning experimental setup is shown in Fig. 7. The outer diameter of the sensing coil is

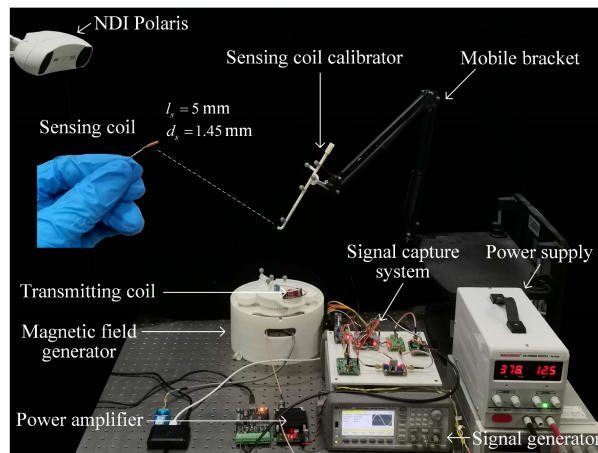


**Fig. 7.** Developed electromagnetic positioning experimental setup.

1.45 mm, the length is 5 mm, and the cavity diameter is 0.8 mm. The cavity can pass stents, drugs, etc. The sensing coil was precisely coaxially fixed with the z-axis of the calibrator to avoid multiple EMFs for one pose. The transmitting coil was mounted on the sun gear of the magnetic field generator. A sinusoidal signal was generated, amplified, and input into the transmitting coil to excite the magnetic field. A Maxon motor driven the transmitting coil with a constant speed. The rotation angle was measured by an encoder with accuracy of 0.176°. The sensing coil was induced in the magnetic field. The sub-millivolt level signal was amplified and filtered by the signal capturer and then collected by a data acquisition card in real-time. The acquisition frequency of the data acquisition card is 100 Hz and the accuracy is 0.3 mV. The sensing coil calibrator is fixed on the end of a 5-DoF mobile bracket.

### B. Microcoil Induced EMF Estimation Experiment

The induced EMF prediction model was evaluated on the experimental setup. The sensing coil manually moved within the workspace. The transmitting coil rotated at a constant speed. Polaris measured the relative pose between the two coils. The calculated features were input into the EMF prediction model. The real EMF was collected by the signal capturer. The experimental results are shown in Fig. 8. Fig. 8(a) displays the motion trajectory of the sensing coil relative to the transmitting coil. The trajectory range is  $x \in [-65, 80]$  mm,  $y \in [-80, 70]$  mm,  $z \in [105, 205]$  mm. 5000 samples were collected. The predicted results, magnetic dipole-based results, and the measured values are shown in the red, green, and blue lines in Fig. 8(b), respectively. Root mean square error (RMSE) of the magnetic dipole-based results is 4.30 mV, the maximum error is 22.64 mV. The local enlarged images show that the EMF prediction deviation of the theoretical calculation results is obvious when the coils were outside a certain range. The proposed EMF prediction model performed better. RMSE of the proposed prediction model is 2.82 mV, the maximum error is 10.36 mV. It improves the accuracy by 34.4% compared with the theoretical model. Fig. 8(c) shows the box plot of the model prediction error for

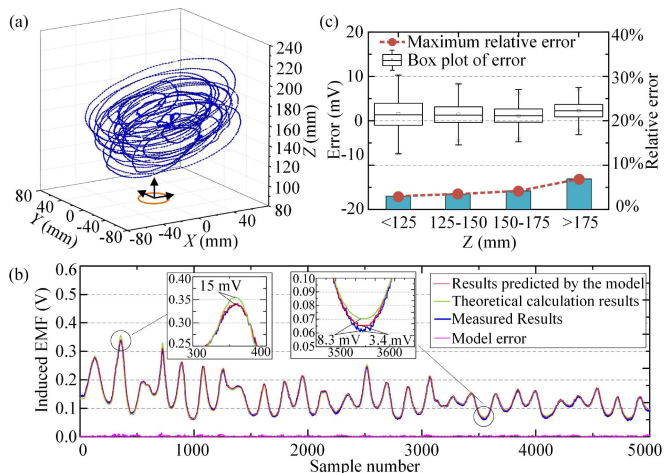


**Fig. 8.** Induced EMF prediction model evaluation experimental results. (a) The sensing coil motion trajectory relative to the transmitting coil collected by NDI Polaris. (b) Induced EMF prediction results. (c) The influence of the  $Z$ -direction distance between the two coils on the prediction error.

different height ranges of sensor coil. The results show that most prediction errors are in the  $\pm 5$  mV range. As the height increased, the error fluctuation range becomes smaller. It is because the magnetic flux intensity decreased. However, the increased maximum relative error will reduce the positioning accuracy. Therefore, the height of the workspace is set below 175 mm.

### C. Positioning Performance Evaluation Experiment

To evaluate the estimation accuracy of the positioning model, a sensing coil set to vertical and horizontal poses was positioned in the workspace. Three planes with heights of 100 mm, 135 mm, and 160 mm were selected. On each plane, 16 points with an interval of 20 mm were selected along the two coordinate axes. Fig. 9(a) shows the 48 selected points and 96 poses. The rotation speed of the transmitting coil can affect the acquisition of the input data sequence. Therefore, the experiments were divided into four groups with different speeds: 3.8 r/min, 11.3 r/min, 18.9 r/min, and 23.6 r/min. Four groups of accuracy evaluation experiments were implemented to verify the speed characteristics, and the averages of the model's stable output values were taken as the estimation results. The experimental results show that there is an offset angle between the estimated pose and the reference pose, and it increases almost linearly with the increase of the rotation speed, as shown by the red marks in Fig. 9(c). The hysteresis offset angles can be caused by the communication delay between the encoder, the signal capturer and the PC. After correcting the offset angles, the localization and orientation estimation accuracy of the four groups is shown in Fig. 9(b). The results show that as the rotation speed increases, the difference in estimation accuracy is not significant, but the response delay decreases significantly, as shown by the blue marks in Fig. 9(c). When the transmitting coil speed was 23.6 rpm, the delay was 0.776 s. Higher speeds require higher

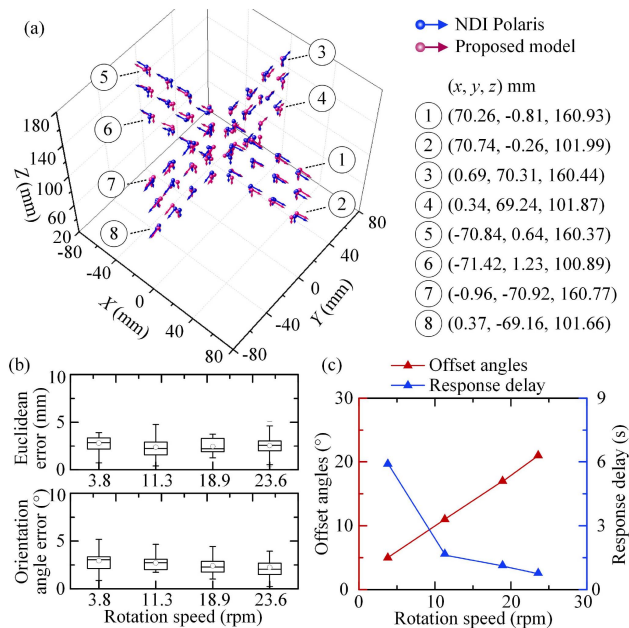


**Fig. 9.** Positioning accuracy and speed characteristics evaluation. (a) Positioning accuracy. (b) Experimental results of the 5-DoF positioning model at four rotation speeds. (c) Offset angles and response delay of four groups.

acquisition frequencies for the encoder. In the future, while ensuring measurement accuracy, encoders with higher baud rates can be employed to increase the speed of the transmitting coil and reduce the delay. Fig. 9(a) shows the results at a rotation speed of 23.6 rpm. The blue arrows represent the poses measured by NDI Polaris, and the red arrows represent the poses estimated by the proposed model. The results show that the static MAEs are  $x_{MAE} = 1.27$  mm,  $y_{MAE} = 1.41$  mm,  $z_{MAE} = 1.20$  mm,  $m_{MAE} = 0.019$ ,  $n_{MAE} = 0.022$ ,  $p_{MAE} = 0.016$ , and the RMSEs are  $x_{RMSE} = 1.55$  mm,  $y_{RMSE} = 1.68$  mm,  $z_{RMSE} = 1.40$  mm,  $m_{RMSE} = 0.025$ ,  $n_{RMSE} = 0.029$ ,  $p_{RMSE} = 0.020$ . Euclidean error is 2.53 mm, orientation error is  $2.24^\circ$ . Another 104 poses were further localized, and the experimental results are shown in Fig. 10(a). The estimated parameter ranges are  $x[-80, 80]$  mm,  $y[-80, 80]$  mm,  $z[95, 170]$  mm,  $m[-1, 1]$ ,  $n[-1, 1]$ ,  $p[-1, 0]$ . It contains the designed workspace. The linearities of the estimated parameters are 3.2%, 3.0%, 4.0%, 3.7%, 4.1%, and 2.9%, respectively, and the model output and input conform to the linear characteristics. To verify the repeatability of the model estimation, three points were randomly selected in the workspace and 10 repeatability positioning experiments were carried out. The results indicate that the type A uncertainty of each parameter is 0.072 mm, 0.050 mm, 0.021 mm,  $0.037^\circ$ ,  $0.041^\circ$ , and  $0.036^\circ$ , which are at a low level. The sample variance is used to evaluate the stability of the model [9]. The sensing coil was placed at point  $(-10$  mm,  $0$  mm,  $102$  mm,  $-0.99$ ,  $-0.05$ ,  $-0.12)$  and positioned by the model for 1000 times, as shown in Fig. 10(b). The calculated sample variances of the parameters are  $x_s^2 = 0.012$ ,  $y_s^2 = 0.026$ ,  $z_s^2 = 0.003$ ,  $m_s^2 = 2.8 \times 10^{-7}$ ,  $n_s^2 = 2.1 \times 10^{-6}$ ,  $p_s^2 = 2.5 \times 10^{-6}$ . The results show that the fluctuation of the model estimation is insignificant.

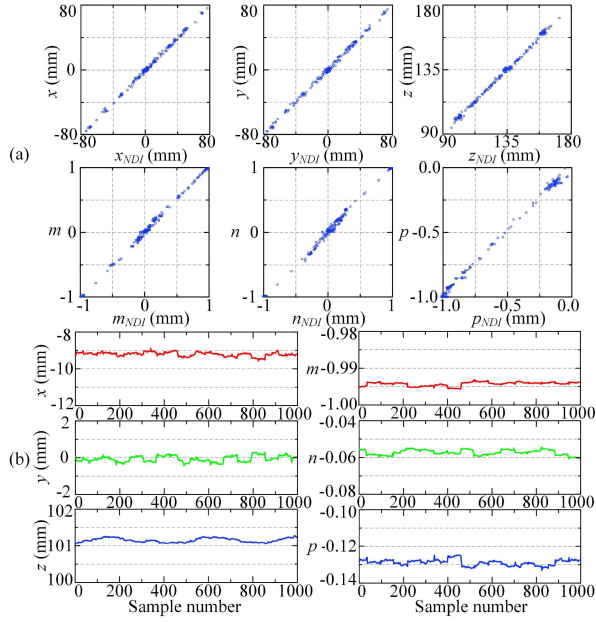


Fig. 10. Linearity and stability evaluation. (a) Linearity. (b) Stability at point (-10 mm, 0 mm, 102 mm, -0.99, -0.05, -0.12).

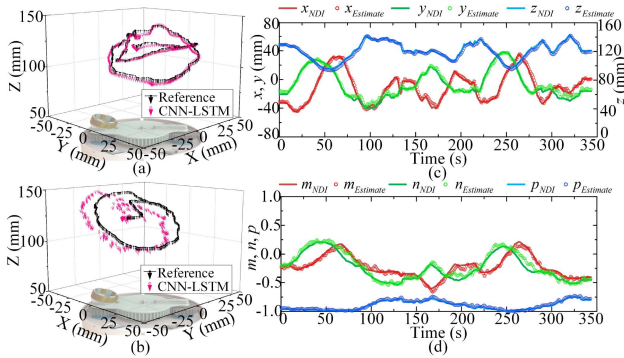


Fig. 11. The experimental group 5-DoF pose tracking results. (a) CNN-LSTM-based positioning model. (b) LM-based positioning model. (c) Euclidean distance tracking accuracy: 4.25 mm. (d) Orientation tracking accuracy: 3.44°.

#### D. 5-DoF Pose Tracking

The performance of 5-DoF pose tracking was experimentally evaluated with the sensing coil simultaneously translated and rotated manually. The reference trajectories were measured by the Polaris. The test trajectories are illustrated in Fig. 11(a) and (b). The experimental group trajectory from 140 to 280 s is shown in Fig. 11(a). The results of control group, estimated by the LM algorithm, are shown in Fig. 11(b). The black trajectories represent the reference trajectories, and the red trajectories represent the estimated trajectories.

Fig. 11(c) and (d) display the results of experimental group. The displacement range of the trajectory was  $x[-45, 36]$  mm,  $y[-40, 39]$  mm,  $z[95, 143]$  mm. The orientation range was  $m[-0.60, 0.22]$ ,  $n[-0.53, 0.22]$ ,  $p[-1.00, -0.75]$ . The total length of the trajectory was 844 mm and the rotation about all

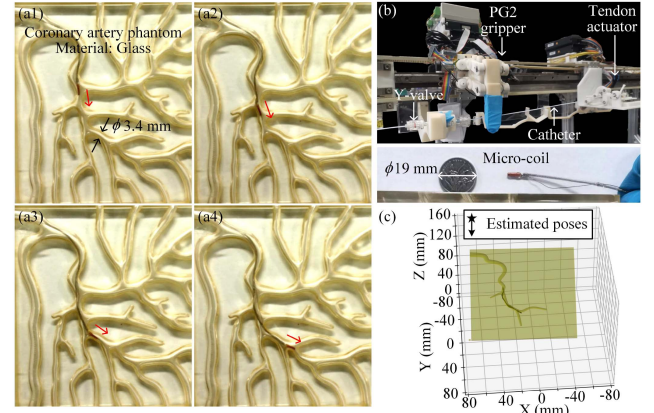


Fig. 12. Navigation experiment in vascular phantom. (a1)–(a4) Inserting the catheter into a vascular phantom. (b) The VIS robotic system and the catheter embedded with a microcoil. (c) Virtual navigation interface.

TABLE V  
PERFORMANCE OF 5-DOF POSE TRACKING

	Error Type	MAE	
		LM	CNN-LSTM
Localization error (mm)	X	7.84	<b>2.28</b>
	Y	6.30	<b>2.37</b>
	Z	2.68	<b>1.68</b>
	Euclidean distance	11.22	<b>4.25</b>
Orientation error (°)	Angle with X-axis	11.36	<b>1.89</b>
	Angle with Y-axis	10.20	<b>2.39</b>
	Angle with Z-axis	7.92	<b>2.27</b>
	Angle error	15.68	<b>3.44</b>

Bold entries represent that the CNN-LSTM-based positioning model has better pose tracking accuracy.

three axes were covered. The results indicate the pose estimates generally follow the true poses well. The pose tracking errors are also summarized in Table V. The MAEs of localization errors in all directions are below 2.5 mm and the Euclidean distance error is 4.25 mm. The MAEs of orientation errors in all directions are below 2.5° and the angle error is 3.44°. It improves the localization and orientation accuracy by 62% and 78%, respectively, compared to the LM algorithm. The prediction delay exists in the dynamic tracking process, so the tracking error is slightly larger than the static error of 2.54 mm and 2.24° in Fig. 9(a). Due to factors such as processing quality, the tracking accuracy is worse than the complex NDI Aurora electromagnetic positioning system ( $\phi 0.92 \times 5.5$  mm, localization error: Less 2 mm, orientation error: less 1°). It has better accuracy than existing permanent magnet-based positioning sensors with larger sizes (Elliptic cylinder with height of 40 mm, a major-axis length of 16 mm and a minor-axis length of 8 mm, localization error: 5.83 mm, orientation error: 4.91° [21]). The proposed positioning system has advantages in terms of sensor size and accuracy.

#### E. Navigation Experiment in Vascular Phantom

A navigation experiment in a coronary artery phantom was performed to verify the usability of the positioning system in

narrow vascular tracts. The sensing coil was embedded in the tip of the steerable catheter, as shown in the Fig. 12(b). The experiment used a hard glass coronary phantom. The length and diameter of the sensor would limit its passability. We designed a virtual visual interface that can synchronously display the predicted sensor poses in the 3-D virtual model, as shown in Fig. 12(c). The operator used the VIS robot to gradually insert the catheter into the coronary artery, as shown in Fig. 12(a1)–(a4). The diameter of the target vessel is 3.4 mm. The predicted trajectory of the microcoil is shown in Fig. 12(c). By observing the 3-D visual interface, the operator can easily identify the pose of the catheter tip, thereby navigating the surgical operation. The application experiment results demonstrated the potential of the positioning system for use in narrow tracts.

## V. CONCLUSION

This article proposed a novel 5-DoF electromagnetic positioning system utilizing rotating single-axis electromagnetic field excitation coil to locate the microcoil with a size of  $\phi 1.45 \times 5$  mm. To this aim, an XGBoost-based induced EMF prediction model is proposed to correct the deviation of the magnetic dipole model in near excitation source. The experimental results indicate that the EMF prediction accuracy of the model is 34.4% higher than that of the magnetic dipole model. To solve the problems that the existing iteration methods, such as LM algorithm, are sensitive to initial values and has poor iteration robustness, a 5-DoF positioning model based on neural network is designed. A model-based dataset generation method is proposed, reducing the difficulty and workload of dataset collection. Combining the spatial feature capture capability of CNN and the sequence feature capture capability of LSTM, a CNN-LSTM-based positioning model is designed and trained. Then the electromagnetic positioning model was evaluated experimentally. The results show that the static average localization error is 2.53 mm and the orientation error is  $2.24^\circ$  within the  $\phi 150 \times 70$  mm volume. And the system performance in linearity, uncertainty, and stability was quantitatively evaluated using metrological indicators. To validate the speed characteristics, four experiments with varying transmitting coil rotation speeds were conducted. They reveal that the angle offset is proportional to the speed and the predicted delay rapidly decreases as the speed increases. The dynamic tracking experimental results demonstrate that the proposed positioning model has a localization tracking error of 4.25 mm and an orientation tracking error of  $3.44^\circ$ , representing improvements of 62% and 78% over the LM algorithm, respectively. Finally, the positioning system was applied to catheterization navigation in a coronary artery phantom, demonstrating its effective penetrating positioning function in narrow lumens. In the future, steerable catheters embedded with multiple microcoils will be developed. Leveraging CT images, it holds the potential for autonomous navigation within blood vessels.

## REFERENCES

- [1] S. Sharma et al., "Wireless 3D surgical navigation and tracking system with 100  $\mu\text{m}$  accuracy using magnetic-field gradient-based localization," *IEEE Trans. Med. Imag.*, vol. 40, no. 8, pp. 2066–2079, Aug. 2021.
- [2] X. Bao et al., "Multilevel operation strategy of a vascular interventional robot system for surgical safety in teleoperation," *IEEE Trans. Robot.*, vol. 38, no. 4, pp. 2238–2250, Aug. 2022.
- [3] X. Bao, S. Guo, C. Yang, and L. Zheng, "Haptic interface with force and torque feedback for robot-assisted endovascular catheterization," *IEEE/ASME Trans. Mechatron.*, vol. 29, no. 2, pp. 1111–1125, Apr. 2024.
- [4] Y. Yan et al., "Machine learning-based surgical state perception and collaborative control for a vascular interventional robot," *IEEE Sensors J.*, vol. 22, no. 7, pp. 7106–7118, Apr. 2022.
- [5] M. Zhang, L. Yang, C. Zhang, Z. Yang, and L. Zhang, "A 5-D large-workspace magnetic localization and actuation system based on an eye-in-hand magnetic sensor array and mobile coils," *IEEE Trans. Instrum. Meas.*, vol. 72, 2023, Art. no. 7501411.
- [6] K. Li, Y. Xu, Z. Zhao, A. Li, and M. Q.-H. Meng, "Closed-loop magnetic manipulation for robotic transesophageal echocardiography," *IEEE Trans. Robot.*, vol. 39, no. 5, pp. 3946–3959, Oct. 2023.
- [7] Q. Zhang, Y. Li, H. Xu, X. Li, and X. Zhang, "Magnetic localization method of capsule endoscope based on hybrid model," *IEEE Trans. Instrum. Meas.*, vol. 72, 2023, Art. no. 4003710.
- [8] Q. Lu, Y. Zhang, J. Lin, and M. Wu, "Dynamic electromagnetic positioning system for accurate close-range navigation of multirotor uavs," *IEEE Sensors J.*, vol. 20, no. 8, pp. 4459–4468, Apr. 2020.
- [9] W. Yang, C. Zhang, H. Dai, C. Hu, and X. Xia, "A novel wireless 5-D electromagnetic tracking system based on nine-channel sinusoidal signals," *IEEE/ASME Trans. Mechatron.*, vol. 26, no. 1, pp. 246–254, Feb. 2021.
- [10] D. von Arx, C. Fischer, H. Torlakcik, S. Pané, B. J. Nelson, and Q. Boehler, "Simultaneous localization and actuation using electromagnetic navigation systems," *IEEE Trans. Robot.*, vol. 40, pp. 1292–1308, 2024.
- [11] C. Vergne et al., "Low-field electromagnetic tracking using 3-D magnetometer for assisted surgery," *IEEE Trans. Magn.*, vol. 59, no. 2, 2023, Art. no. 5400205.
- [12] P. Zhong, J. Zhao, Z. Yuan, W. Zhao, T. Zhang, and Y. Feng, "A novel electromagnetic positioning prototype system with simplified receiver for interventional surgery application," *IEEE Internet Things J.*, vol. 10, no. 11, pp. 9753–9767, Jun. 2023.
- [13] X. Wu, S. Song, and J. Wang, "Calibration-by-pivoting: A simple and accurate calibration method for magnetic tracking system," *IEEE Trans. Instrum. Meas.*, vol. 71, 2022, Art. no. 4005209.
- [14] B. Rivkin et al., "Electronically integrated microcatheters based on self-assembling polymer films," *Sci. Adv.*, vol. 7, no. 51, 2021, Art. no. eabl5408.
- [15] S. Chang et al., "A joint graph-based approach for simultaneous underwater localization and mapping for AUV navigation fusing bathymetric and magnetic-beacon-observation data," *J. Mar. Sci. Eng.*, vol. 12, no. 6, p. 954, 2024.
- [16] Y. Yan, S. Guo, C. Lyu, D. Zhao, and Z. Lin, "A novel steerable catheter for vascular interventional surgery," in *Proc. 2023 IEEE Int. Conf. Mechatron. Automat.*, IEEE, 2023, pp. 766–771.
- [17] Y. Yan, S. Guo, C. Lyu, D. Zhao, and Z. Lin, "SEA-based humanoid finger-functional parallel gripper with two actuators: PG2 gripper," *IEEE Trans. Instrum. Meas.*, vol. 72, 2023, Art. no. 3000213.
- [18] Y. Yan et al., "Grasping force-based passive safety method for a vascular interventional surgery robot system," *IEEE Trans. Instrum. Meas.*, vol. 72, 2023, Art. no. 7506412.
- [19] Y. Lu et al., "A comparison of interpretable XGBoost and artificial neural network model for the prediction of severe acute pancreatitis," *Polish Arch. Intern. Med.*, vol. 134, no. 5, pp. 16700–16708, 2024.
- [20] A. Agga et al., "CNN-LSTM: An efficient hybrid deep learning architecture for predicting short-term photovoltaic power production," *Electric Power Syst. Res.*, vol. 208, 2022, Art. no. 107908.
- [21] S. Liu and H. Wang, "A wireless 6-DoF pose tracking system using a triaxially anisotropic soft magnet," *IEEE/ASME Trans. Mechatron.*, early access, Jul. 06, 2024, doi: [10.1109/TMECH.2024.3422391](https://doi.org/10.1109/TMECH.2024.3422391).



**Yonggan Yan** received the M.S. degree in mechanical engineering from Yanshan University, Hebei, China, in 2021. He is currently working toward the Ph.D. degree in biomedical engineering with the Beijing Institute of Technology, Beijing, China.

He researches on master–slave systems for remote surgical robots.



**Shuxiang Guo** (Fellow, IEEE) received the Ph.D. degree in mechatronics and systems from Nagoya University, Nagoya, Japan, in 1995.

He is currently a Full Professor with Department of Electronic and Electrical Engineering, Southern University of Science and Technology, Shenzhen, China, and Chair Professor with the Beijing Institute of Technology, Beijing, China. His current research includes minimal invasive surgery robot systems and rehabilitation

robotics.

Dr. Guo has a fellowship of the Engineering Academy of Japan.



**Pengfei Yang** received the seven-year program of clinical medicine from the Zhejiang University School of Medicine, Zhejiang, China, in 2007, and the M.D. degree in neurosurgery from the Second Military Medical University, Shanghai, China, in 2013.

He is currently the Executive Director of the Neurovascular Center, Shanghai Changhai Hospital, Shanghai, China, and the Vice Director of Institute of Cerebrovascular Diseases, PLA. His current research interests include

ENCHANTED-2/MT, DIRECT-MT, MAGIC-MT, and LATE-MT.



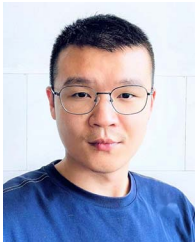
**Bingzhi Shen** received the B.E. degree in electronic information science and technology from Beijing Forestry University, Beijing, China, in 2023. He is currently working toward the M.S. degree in biomedical engineering with the Beijing Institute of Technology, Beijing.

His research interests include surgical robotics, deep learning, and image processing.



**Yongwei Zhang** received the M.S. degree in neurology from the Second Military Medical University, Shanghai, China, in 2011.

He is skilled in the field of neurointerventional treatment with twenty years of experience. He is currently the Vice Director of the Neurovascular Center, Shanghai Changhai Hospital, Shanghai, China. His representative papers have been published in NEJM and the Lancet. His current research interests include ENCHANTED-2/MT, DIRECT-MT, MAGIC-MT, and LATE-MT.



**Chuqiao Lyu** received the B.S., M.S., Ph.D. degrees in biomedical engineering from the Beijing Institute of Technology, China, in 2016, 2019, and 2024, respectively.

He is currently a postdoctoral researcher with Tsinghua Shenzhen International Graduate School (SIGS). He has published 20 academic papers, with research interests encompassing vascular interventional surgical robotics, intravascular sensing technologies, and liquid-solid triboelectric nanogenerators.



**Yongxin Zhang** received the M.D. degree in neurosurgery from the Second Military Medical University, Shanghai, China, and the Ph.D. degree in neurosurgery from the Second Military Medical University, Shanghai, China, in 2017.

He is currently the Secretary of the OCIN Imaging core-lab. His representative papers have been published in NEJM and the Lancet. His current research interests include ENCHANTED-2/MT, DIRECT-MT, MAGIC-MT, and LATE-MT.



**Mingchao Ding** received the M.S. degree in imaging and nuclear medicine from the Peking University School of Medicine, Beijing, China, in 2011.

He is currently the Vice President, Chief Physician, Professor, and Doctoral Supervisor with the Aerospace Center Hospital, and the Head of the Continuing Education and Training Base for Peripheral Vascular Interventional Physicians of the National Health Commission.

His current research interests include endovascular treatment and emergency interventional treatment of ischemic peripheral vascular diseases, bleeding diseases, and thrombotic diseases.



**Jianmin Liu** received the bachelor's degree in clinical medicine from the Second Military Medical University, Shanghai, China, in 1984.

He was a Visiting Professor with Osaka University Medical College, Japan, in 1997. He is currently the Director of the Neurovascular Center, Shanghai Changhai Hospital, Shanghai, China, and the Director of the Institute of Cerebrovascular Disease, PLA. He has authored or coauthored more than 500 papers and edited and co-edited seven monographs. His current

research interests include ENCHANTED-2/MT, DIRECT-MT, MAGIC-MT, and LATE-MT.